Construction of an Anion-Pillared MOF Database and the Screening of MOFs Suitable for Xe/Kr Separation

Chenkai Gu[†,‡], Zhenzi Yu[‡], Jing Liu[*,†], David S. Sholl[*,‡]

[†] State Key Laboratory of Coal Combustion, School of Energy and Power Engineering, Huazhong University of Science and Technology, Wuhan, 430074, China

[‡] School of Chemical and Biomolecular Engineering, Georgia Institute of Technology, Atlanta, GA 30332-0400, USA

ABSTRACT: The separation of xenon/krypton (Xe/Kr) mixtures is a challenging process. Many porous materials allow the adsorption of both Xe and Kr, but only with low selectivity. Anion-pillared MOFs, featuring the anion groups as structural pillars, show potential in gas separations, but only a limited number of them have been synthesized. Here we describe a collection of 936 anion-pillared MOFs based on 22 experimentally available structures. We performed DFT optimization and then assigned DDEC charges for each MOF to make them well suited to many molecular simulations. The structural properties of the MOFs vary more strongly with the choice of the organic ligand than with other aspects like fluorine groups and metal centers. We then screened the entire collection of MOFs in the context of Xe/Kr separation at room temperature. Compared with previously reported MOFs, the interpenetrated MOF SIFSIX-6-Cd-i is predicted to perform better for Xe/Kr separations, with a good balance between working capacity (1.62 mmol/g) and separation selectivity (16.4) at 298 K and 100 kPa. We also found that the heterogeneity of fluorine groups within a MOF can help to enhance Xe working capacity without reducing the Xe/Kr selectivity, suggesting that synthesis of anion-pillared MOFs with mixed fluorine groups may lead to

improved Xe/Kr separations performance.

KEYWORDS: *anion-pillared MOFs, high-throughput screening, molecular simulation, Xe/Kr separation*

■ INTRODUCTION

Metal-organic frameworks (MOFs) are a class of porous materials assembled by inorganic clusters and organic building blocks. Owing to their large internal surface area, adjustable pore size and tunable surface environment, MOFs have shown potential in catalysis, separation, chemical sensing and drug delivery.[1] Anion-pillared MOFs, as a subclass of MOF materials, use anion groups as pillars in their structures. The anion groups can provide selective adsorption sites, and thus make anion-pillared MOFs potential materials for gas separations including the selective capture of acid gas (SO_2, CO_2),[2,3] and the separation of Xe/Kr[4] and light hydrocarbon mixtures[5].

Xe/Kr separation is an important but challenging process in industry. High-purity Xe and Kr widely used in electronics, semiconductors, medicine, electric light sources, gas laser and plasma flow.[6] Cryogenic distillation is the most mature technology currently applied in Xe/Kr separations, but is recognized as energy-intensive and high-cost. Adsorptive separations are an energy-effective alternative technology to distillation.[7] In previous work, researchers have tested some solid porous adsorbent materials such as activated carbons and zeolites for Xe/Kr separation but reported low adsorption capacity and selectivity.[8-10] A number of studies have considered MOFs as adsorbents for this separation. Generally, MOFs can realize selective adsorption of Xe over Kr, but their relatively large pores allow the uptake of both Xe and Kr, thereby inhibiting the separation selectivity. MOF-505 shows high Xe/Kr selectivities of 9 - 10 owing to its small pores and strong adsorption

sites.[11] Recently, breakthrough experiments confirmed that ZU-62 has practical potential for producing high-purity Kr and Xe from air-separation byproducts, showing record Kr productivity (206 mL/g) and Xe productivity (42 mL/g) as well as good recyclability.[12]

Over the past few years a limited number of anion-pillared MOFs have been synthesized and studied for their separation performance.[13] The structure of these materials suggests that a large number of variants are possible, but it would require considerable resources to explore these variants experimentally. This observation motivated us to use modeling to create a database of experimentally plausible anion-pillared MOFs. Using this computation-ready database, detailed simulations and screening work can be carried out to explore various subsequent possible applications of these materials. This approach follows on the success of existing databases constructed to accelerate the modeling of porous materials such as zeolites, polymer, amorphous materials, and MOFs.[14] The Database of Zeolite Structures, managed by the International Zeolite Association (IZA), provides structural information on all zeolite framework types approved by the structure commission.[15] In addition, a very large database of over 800,000 2D zeolite nanosheets has been created based on the full range of known zeolite structures in the IZA database.[16] Recently, Thyagarajan and Sholl reported a database of 205 atomistic models of amorphous nanoporous materials drawn from earlier literature.[17] The Cambridge Structural Database (CSD) consists of more than one million organic and metal-organic crystal structures derived from X-ray or neutron diffraction analyses.[18] Based on the CSD, Chung et al.[19] published the first version of the CoRE-MOF database containing 5,109 experimental MOF structures with pore-limiting diameter greater than 2.4 Å. This database can be directly used in molecular simulations. The recently updated CoRE-MOF database contains over 14,000 structures (CoRE-MOF 2019).[20]

In this work, we constructed an anion-pillared MOF database based on the available structures reported in previous experiments. All MOF structures were optimized with DFT calculations. Although the partial charges are not required for simulating Xe/Kr adsorption, we still assigned the DDEC charges for MOF atoms to facilitate future simulations of gas adsorption with polar molecules. The reliability of models in this database was confirmed by structural comparisons between the DFT-optimized and experimentally available structures. Then, we then performed high-throughput screening to explore these 936 possible MOFs in the context of Xe/Kr separations. Three approximate metrics of separation performance, namely the Henry coefficient ratio, working capacity and regenerability, were combined to form the evaluation criteria for this screening. Based on the screening results, we performed GCMC simulations on six promising MOFs and compared the Xe/Kr selectivity with several MOFs reported previously. Finally, we explore whether allowing heterogeneity in the metal centers or fluorine groups in anion-pillared MOFs offers an additional means to improve Xe/Kr separation performance.

■ MODEL AND METHOD

Structures and Nomenclature. The networks of anion-pillared MOFs were formed by connecting three secondary building units (SBUs): fluorine anion groups, metal centers and organic ligands. The structures were named based on their SBUs. For example, SIFSIX-1-Cu, shown in Figure 1, is comprised of SiF_6^{2-}, 4,4'-bipyridyl (ligand no. 1) and Cu cations. Each Cu atom connects four N atoms from organic ligands and two F atoms from SiF_6^{2-} groups, and the entire framework forms a pcu topology.[21] For interpenetrated structures, an additional letter "i" is given at the end of the name. Given all the anion-pillared MOFs currently known from experiment have the pcu topology the

MOFs we considered were assumed to have the same pcu topologies. Examples certainly exist for other classes of MOFs where structural polymorphs can exist,[22] so we cannot exclude the possibility that anion-pillared MOFs with non-pcu topologies might also exist.

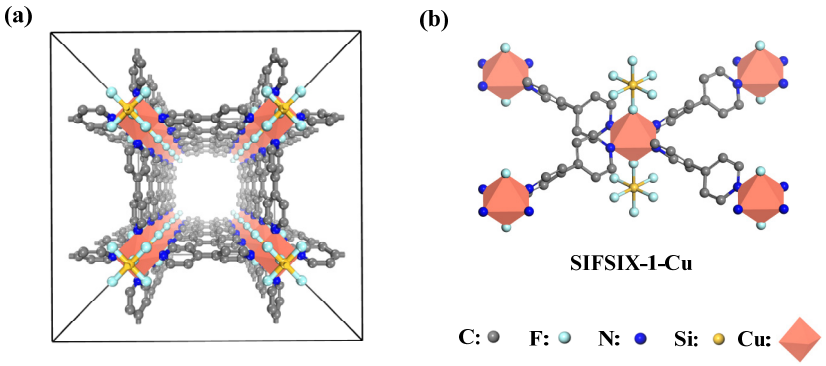

Figure 1: (a) Crystal structure and (b) representative fragment of SIFSIX-1-Cu.

DFT Geometry Optimizations. Geometry optimizations of MOFs were performed with periodic DFT calculations using the Vienna Ab initio Simulation Package (VASP) with projected-augmented wave (PAW) pseudo potentials[23] and a plane-wave basis set.[24] Nazarian et al.[25] evaluated the performance of six different DFT functionals for predicting lattice parameters, unit cell volume, bonded parameters and pore descriptors of MOFs and reported that PBE-D2, PBE-D3, and vdW-DF2 give more accurate predictions on average than similar calculations without dispersion corrections. Therefore, all geometry optimizations in this work used the Perdew-Burke-Ernzerhof (PBE) generalized gradient approximation (GGA) exchange-correlation functional[26] with D3 dispersion corrections (PBE-D3).[27] Lattice parameters and atomic positions were relaxed using a plane-wave cutoff energy of 600 eV. Γ-point sampling method was used in reciprocal space. Geometry optimizations were performed with a conjugate gradient algorithm until forces on each atom were <0.05 eV/Å. We used DFT+U to describe the strength of on-site Coulomb interactions for localized electrons with Hubbard *U* corrections for Ti (3.0), Zr (4.0), V (3.1), Nb (1.5), Fe (4.0), Co (3.4), Ni

(6.0) and Cu (4.0).[28,29] In our DFT+U calculations *J* was set as zero for all atoms. Spin polarization was also considered by including initial ferromagnetic state for Fe, Co, Ni and Cu atoms.

For a limited number of examples, adsorption energies for Xe and Kr were computed with periodic DFT calculations. These calculations used the PBE-D3 functional, which was the best performing among the nine functionals with respect to DFT/CC according to Grajciar et al.[30] The binding energies of gas molecules (Xe and Kr) in MOFs were defined by

$$\Delta E = E_{gas+MOF} - E_{gas} - E_{MOF} \quad (1)$$

where $E_{gas+MOF}$, E_{gas} and E_{MOF} represent the energy of entire gas-MOF interaction system, the energy of gas molecule and the energy of empty MOF, respectively. Here, ΔE is negative when adsorption is exothermic.

Molecular Simulations. The adsorption of pure gases and Xe/Kr mixtures were calculated with grand canonical Monte Carlo (GCMC) simulations. MOF atoms were held rigid at their DFT-optimized crystallographic positions in these simulations. A cutoff radius of 12 Å was used for van der Waals (vdW) interactions. Periodic boundary conditions were applied in three dimensions and supercells were chose to ensure that the simulation volume was larger than twice the cutoff radius for vdW interactions in each dimension. Each state point used 2.5×10^5 initialization cycles for equilibration and 5×10^5 cycles for thermodynamic properties calculation. Preliminary tests indicated these parameters gave well converged results. All GCMC simulations were carried out using RASPA.[31]

Gas-gas and gas-MOF interactions were modeled as purely van der Waals (vdW) interactions with the Lennard-Jones (L-J) form

$$E_{FF}(r_{ij}) = E_{vdw} = 4\varepsilon_{ij}\left[\left(\frac{\sigma_{ij}}{r_{ij}}\right)^{12} - \left(\frac{\sigma_{ij}}{r_{ij}}\right)^{6}\right] \quad (2)$$

where r_{ij}, σ_{ij} and ε_{ij} represents the interatomic distance, the repulsion distance and the potential well depth between atom i and j, respectively. The L-J parameters for Xe and Kr were taken from Hirschfelder et al.[32] and Talu and Myers,[33] respectively. For framework atoms, the L-J parameters were taken from the Universal Forcefield (UFF)[34] for transition metal atoms and DREIDING[35] forcefield for other atoms.

■ RESULTS AND DISCUSSION

3.1 Construction of Structure Database

Establishment of Initial Model. We generated a large set of chemically plausible hypothetical anion-pillared MOF structures. To do this, we first collected a set of 22 anion-pillared MOF structures that have previously been reported experimentally, [4,21,36-49] as shown in Table S2. These structures included the 8 fluorine groups, 5 metal centers and 12 organic linkers as shown in Figure 2. The name of each ligand is listed in Table S3. To broaden the range of materials under consideration, we also include one additional metal center (Cd) and four additional fluorine groups (VOF_5^{2-}, BF_5^{2-}, GaF_5^{2-}, InF_5^{2-}) because they are chemically analogous to examples from Figure 2. Predictions about possible interpenetrations of the MOFs were made by comparison with the available experimental data. The long ligands (ligands 4 - 6 and 13 - 16) have only been observed experimentally to form interpenetrated structures,[36,38,41,43,45,47] so we assumed this was the case for all combinations of metals and fluorine groups with these ligands. Similarly, we assumed ligands 1, 3, 7 and 18 only form non-interpenetrated structures. Ligand 2 has been found experimentally to give both interpenetrated and non-interpenetrated structures,[13,39] so both cases were considered for all materials with this ligand. The approach outlined above generated 936 different MOFs, as listed in Table S5.

To ensure accurate geometries for each material, plane wave DFT calculations were performed to energy minimize each structure. We then calculated DDEC charges[50] for each atom in the optimized MOFs. Information on the full collection of optimized structures is available in the Supporting Information.

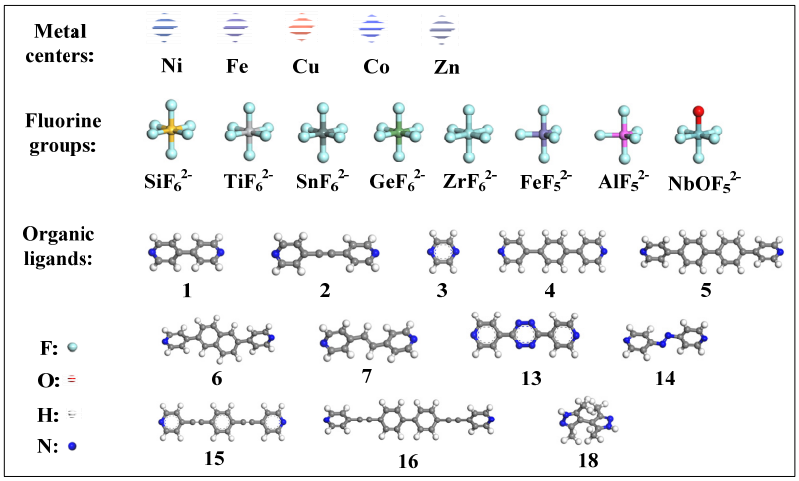

Figure 2: Collection of metal centers, fluorine groups and organic ligands in all of anion-pillared MOFs reported previously experimentally.

Figure 3(a) compares the DFT-optimized unit cell parameters for the anion-pillared MOFs in Table S2 to the corresponding experimental structures. The mean absolute deviation (MAD) for the relative unit cell volumes, V_{DFT}/V_{exp}, for these 20 structures was 3.0%. The good agreement between the DFT predictions and experimental data is similar to that observed by Nazarian et al. for a diverse test-set of MOF structures.[25] The structural differences of MOFs in our database can be mainly attributed to variations in metal-fluorine bond lengths, as shown in Figure 3(b). The mean absolute deviation (MAD) for the relative bond length (L_{DFT}/L_{exp}) of the 20 structures was 3.4 %.

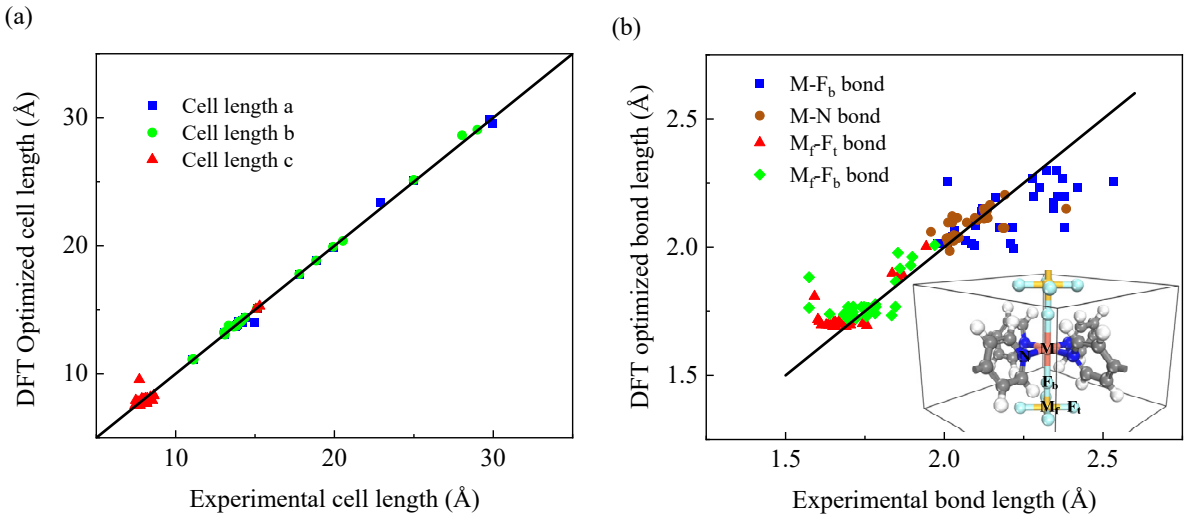

Figure 3: Comparisons of (a) cell lengths and (b) bond lengths between DFT optimized results and experimental data for 22 anion-pillared MOFs. A parity line is shown in each panel. Numerical data is listed in Table S4.

Analyses of the Structural Parameters. Figure 4 shows physical descriptors for all MOFs from the database in a pairwise fashion, including accessible surface area (ASA) vs. density, probe-accessible vs. probe-occupiable volume fraction and pore limiting diameter (PLD) vs. its difference with LCD (largest cavity diameter). The corresponding values are available in Table S5. All the physical descriptors were computed using zeo++[51] based on the DFT-optimized structures. A probe radius of He (1.3 Å) were applied when calculating ASA, probe-accessible and probe-occupiable volume fraction.

In this database the materials have nonzero volumetric ASAs ranging from 217 to 2676 m^2/cm^3. Some of these MOFs have the same molecular formula but different physical parameters. For example, interpenetrated MOFs like SIFSIX-2-Cu and SIFSIX-2-Cu-i have the same elemental stoichiometry, but differ strongly in density (0.632 and 1.240 cm^3/g), He ASA (2250 and 1271

m^2/cm^3), probe-accessible volume fraction (0.392 and 0.033), probe-occupiable volume fraction (0.655 and 0.235), PLD (10.37 and 3.59 Å) and LCD (11.30 and 3.83 Å). Some of the frameworks, for example NbOFFIVE-14-Co-i, have zero or near-zero porosity owing to their very limited pore sizes. The above phenomenon can also be observed in other MOFs[19,20] and in a recent database of porous amorphous materials.[17] The probe-occupiable volume is the total pore volume occupied by the entire probe molecule rather than the space just accessible to the center of probe molecule, which leads to a higher volume fraction. The pore limiting diameter (PLD) is the maximum size for the molecular diffusion without steric hindrance of structural atoms in MOFs or local deformation of the MOFs. The largest cavity diameter (LCD) indicates the largest size of probe molecule that can be inserted at any region inside the MOFs. By definition, the LCD is higher than the PLD in value, so we plotted the PLD against the difference between the LCD and PLD in Figure 4(c).

In order to understand the effects of SBUs on MOF structures, we created four groups in which materials differ only in the identity of fluorine groups, metal centers, or organic ligands or by the presence/absence of interpenetration. These four groups are shown with colored symbols in Figure 4. For example, group 1 contains 12 MOFs with different fluorine groups but the same metal center (Cu) and organic ligand (ligand 7). The MOFs contained in each group are listed in Table S6. The results in Figure 4 show that the structural properties vary more strongly with the choice of the organic ligand than with other aspects of the MOFs. The accessible surface area can be varied from ~1000 to 2500 m^2/cm^3 with a step size of ~200 m^2/cm^3 by varying the organic ligand (see green symbols in Figure 4(a)). Changing the fluorine groups (red symbols in Figure 4(a)) or metal centers (blue symbols in Figure 4(a)) of MOFs, the accessible surface area can be varied by ~40 m^2/cm^3.

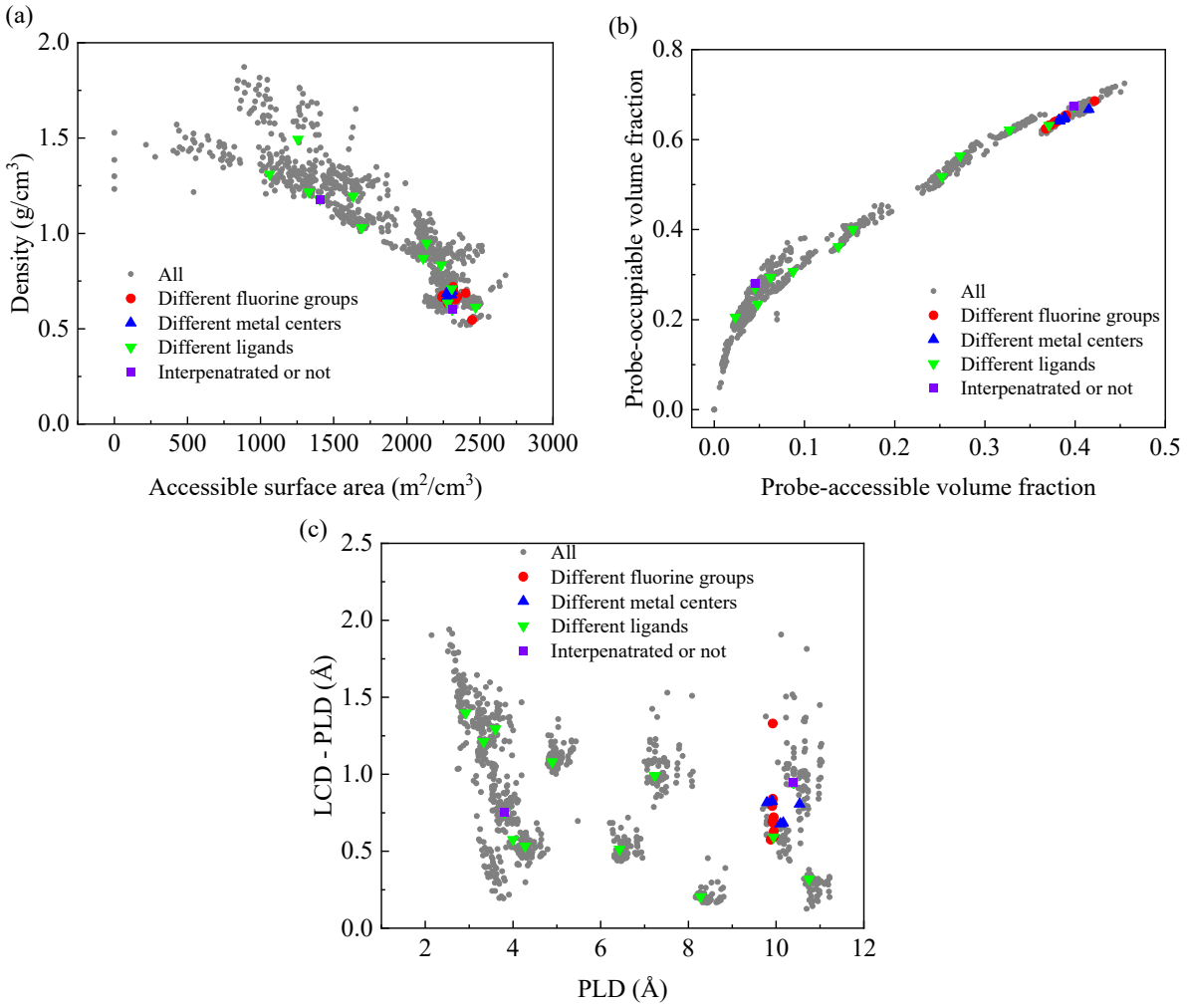

Figure 4: Physical parameters of all anion-pillared MOFs in the database shown as gray solid circles. (a) He-probe accessible surface area (ASA) vs. density; (b) probe-accessible vs. probe-occupiable volume fraction (He probe); (c) PLD vs. LCD - PLD. The colored symbols represent four groups which differ only in their fluorine groups, metal centers, organic ligands and structural interpenetrations, respectively.

3.2 Screening of MOFs for Xe/Kr Separation

Validation of Force Field. To assess the accuracy of the force field used to describe gas adsorption, adsorption energies from molecular simulations and DFT calculations were compared for

representative examples. The interaction energies of single Xe or Kr molecules in SIFSIX-6-Cd-i and ALFFIVE-3-Cd were calculated by DFT (PBE-D3) and compared with the corresponding force field-based adsorption energies as shown in Figure 5. Similar to previous work,[52-54] we generated 100 configurations randomly for each adsorbed molecule in each MOF through NVT MC (N = 1, T = 298 K) simulations. The DFT calculations span interaction energy ranges of -25 ~ -17 kJ/mol for Kr in ALFFIVE-3-Cd, -33 ~ -26 kJ/mol for Xe in ALFFIVE-3-Cd, -21 ~ -13 kJ/mol for Kr in SIFSIX-6-Cd-i and -30 ~ -22 kJ/mol for Xe in SIFSIX-6-Cd-i. As might be expected, both MOFs adsorb Xe more strongly than Kr. Figure 5(b) shows the deviations between force field and DFT energies for all 400 snapshots. 393/400 (98.25%) of these deviations locate within ±2.5 kJ/mol, indicating the force field is well suited to describing adsorption of these rare gas atoms in these MOFs.

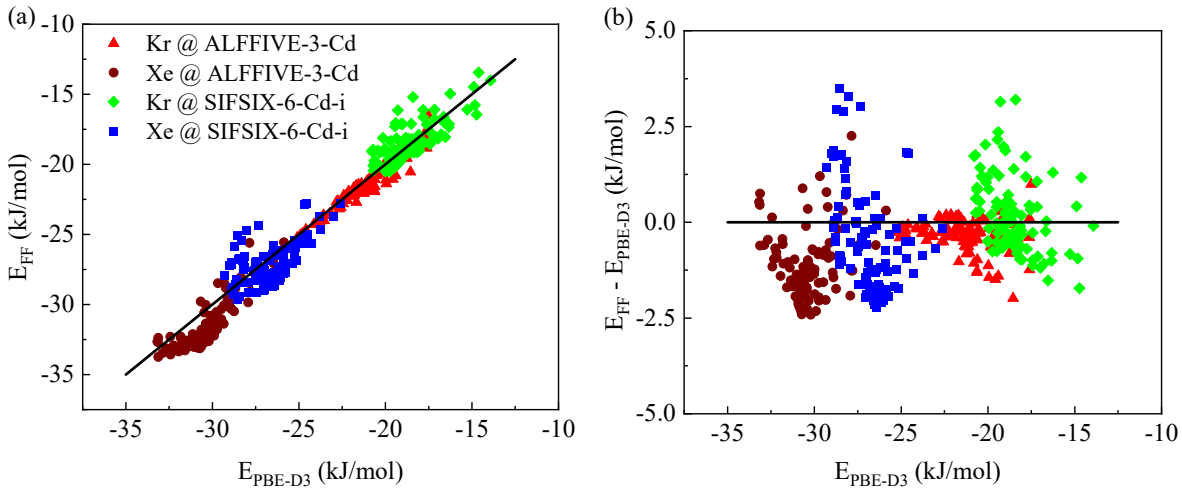

Figure 5: (a) Comparison of the interaction energies of Xe and Kr in ALFFIVE-3-Cd and SIFSIX-6-Cd-i for force field and DFT (PBE-D3). (b) The interaction energy difference ($E_{FF} - E_{PBE-D3}$) as a function of E_{PBE-D3}.

Screening Based on Henry Coefficient Ratio, Working Capacity and Regenerability. To consider the large number of structures in our collection as potential materials for Xe/Kr separations, it is useful to calculate several approximate metrics of separation performance.[55-58] The ratio of Henry's coefficient of pure Xe and Kr, $K_H(Xe)/K_H(Kr)$, was used to evaluate the adsorption selectivity of our MOFs. In the limit of dilute loadings this ratio is, without approximation, the adsorption selectivity.[59] The Henry's constant for each gas was computed in each material using Widom insertion as implemented in RASPA. Working capacity and regenerability metrics were calculated to give additional insight into the potential of each material practical application. The working capacity is calculated by the loading difference of pure Xe at 10 and 100 kPa at 298 K. To estimate the Xe loading at these two pressures, we followed the approach of Tang et al.,[60] which assumes the adsorption isotherm has the Langmuir form

$$q(P) = \frac{KP}{1+\frac{KP}{q_{sat}}} \quad (3)$$

where the K and q_{sat} represent the Henry's coefficient and the saturation loading. Instead of performing molecular simulations to establish the saturation loadings, q_{sat} was estimated by $q_{sat}(r) = k(r)\rho_{liq}f(r)$. Here, ρ_{liq} is the critical density of Xe (1.10 g/cm^3). $k(r)$ is the scaling factor with a probe radius of r. The $k(r)$ and r values of many molecules are available in previous work by Tang et al.[60] For Xe the values of $k(r)$ and r are 1.26 and 0.61, respectively. $f(r)$ is the void fraction and was calculated by zeo++[51] with a probe radius of r.

We also calculated the Xe saturation loadings of a selection of MOFs with GCMC simulations and compared these results with the predictions of the approximate method described above. The Xe saturation loadings were estimated by the Xe uptake at 298 K and 50 bar (see Figure S1 and Table S7). This comparison indicates that the approximate method provides reasonable results.

We used the approximate isotherms to calculate the regenerability, which is defined by the percentage of extractable Xe at 10 kPa relative to the adsorbed Xe at 100 kPa: $(q_{100\ kPa} - q_{10\ kPa})/q_{100\ kPa} \times 100\%$. This parameter evaluates the percentage of the adsorption sites that are regenerable during the desorption process.[61] These metrics cannot give the same level of information that can be obtained from detailed process-level models, but they are a useful initial way to consider a large number of materials.[55]

The performance metrics for each of the 936 DFT-optimized MOFs in our collection are summarized in Figure 6. Generally, the MOFs with higher Xe/Kr selectivity show lower working capacity and regenerability (see Fig. 6(a) and (b)). For example, ALFFIVE-3-Fe (No. 52) has the highest Xe/Kr Henry coefficient ratio (41.5) of any material but its working capacity and regenerability are among the lowest range with values of 0.096 mmol/g and 3.7%, respectively,. GaFFIVE-3-Fe (No. 286), SIFSIX-3-Cd (No. 595) and ALFFIVE-3-Cd (No. 49) have larger working capacity (0.13 mmol/g, 0.19 mmol/g, 0.32 mmol/g) and regenerability (5.3%, 8.1%, 11.0%) but their Xe/Kr Henry's coefficient ratio (33.7, 32.5, 29.2) are lower. By contrast, SIFSIX-6-Cd-i (No. 613) and NbOFFIVE-4-Zn-i (No. 528) have much higher working capacity (1.20 mmol/g, 1.47 mmol/g) and regenerability (32.2%, 67.2%), but moderate selectivity (19.3, 15.6). These tradeoffs illustrate why simply choosing a "winning" material based on a single performance metric is unlikely to be satisfactory.

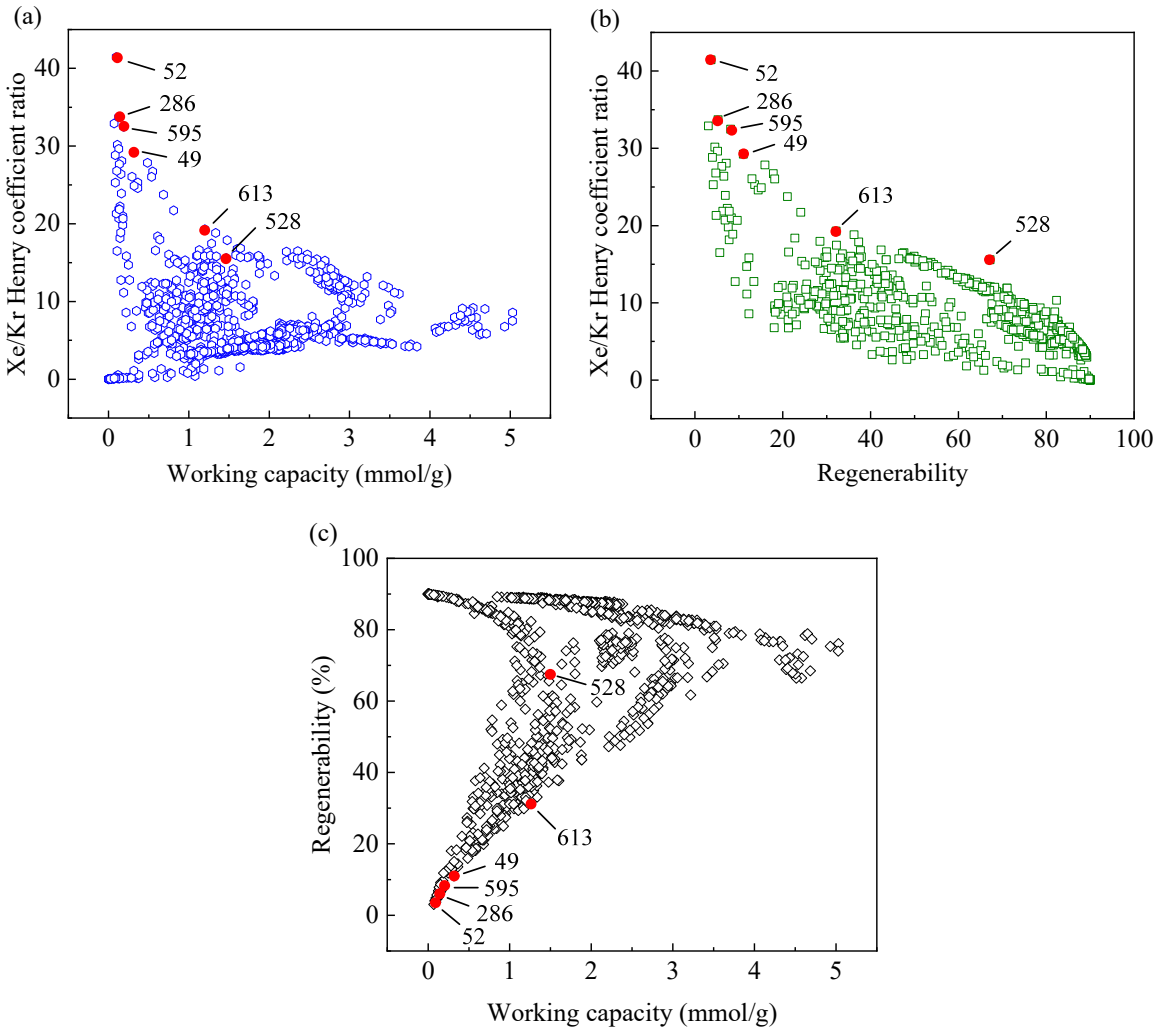

Figure 6: Pairwise comparisons of three performance metrics for Xe/Kr separations in 936 DFT-optimized MOFs: (a) Xe/Kr Henry coefficient ratio as a function of working capacity, (b) Xe/Kr Henry coefficient ratio as a function of regenerability, (c) regenerability as a function of working capacity. Five representative examples, No. 52 ALFFIVE-3-Fe, No. 286 GaFFIVE-3-Fe, No. 595 SIFSIX-3-Cd, No. 49 ALFFIVE-3-Cd, No. 613 SIFSIX-6-Cd-i and No. 528 NbOFFIVE-4-Zn-i, are highlighted. All numerical data in this figure is listed in Table S5.

3.3 Molecular Simulations of Xe/Kr Separations in MOFs

GCMC Simulation of Xe/Kr Separations in the Six Typical MOFs. The working capacity and regenerability metrics considered above relied on estimates of the single-component isotherms rather than detailed molecular simulation data. It is therefore useful to look in more detail at a number of examples to understand the prospects of these materials for Xe/Kr simulations. To this end, GCMC simulations for adsorption of Xe/Kr mixtures were carried out to evaluate the Xe/Kr separation performance at 0.1 – 100 kPa and 298 K of the six MOFs highlighted in Fig. 6. The results of these mixture GCMC simulations are shown in Figure 7. Some but not all of the materials shown in Figure 7 have a maximum in selectivity as pressure is increased. In ALFFIVE-3-Fe, GaFFIVE-3-Fe and SIFSIX-3-Cd the difference between the heat of adsorption for Xe and Kr in the adsorbed mixtures increases as a function of pressure (see Figure S2). In these examples, the difference between heats of adsorption dominates at low pressures but at sufficiently high pressures Kr adsorption becomes more entropically favored, leading to a decrease in the overall selectivity.

The ordering of the materials by selectivity, ALFFIVE-3-Fe > GaFFIVE-3-Fe > SIFSIX-3-Cd > ALFFIVE-3-Cd > SIFSIX-6-Cd-i > NbOFFIVE-4-Zn-i, is the same as given by the Henry's coefficient ratios in Figure 6. Because of the variation in the selectivities with pressure, SIFSIX-6-Cd-i and NbOFFIVE-4-Zn-i show higher selectivities than SIFSIX-3-Cd and ALFFIVE-3-Cd at 100 kPa. The Xe loadings from Xe/Kr mixtures are shown as red lines in Figure 7. The Xe loading reaches saturation in ALFFIVE-3-Fe at very low pressure. That means there is no obvious change in Xe loading for ALFFIVE-3-Fe with pressure between 10 kPa and 100 kPa, consistent with the low working capacity and regenerability estimates in Fig. 6. In contrast, the Xe isotherm for NbOFFIVE-4-Zn-i is much less flat, giving a higher working capacity and

regenerability. The Xe isotherms decline in steepness in the order of ALFFIVE-3-Fe > GaFFIVE-3-Fe > SIFSIX-3-Cd > ALFFIVE-3-Cd > SIFSIX-6-Cd-i > NbOFFIVE-4-Zn-i, which is the same as the sequence predicted by the results in Fig. 6.

We also compared the selectivities, Henry coefficient ratios and working capacities of these six MOFs with those reported in previous work, as shown in Table 1. The selectivities of the six anion pillared MOFs we considered are higher than that of some very well-known MOFs like Cu-BTC and Ni-MOF-74. As emphasized by Figure 6 and 7, however, selectivity alone is likely to be insufficient for determining which materials will perform the best in realistic applications where considerations of working capacity and other factors are also important. In Table 1, $[Co_3(C_4O_4)_2(OH)_2]$ has the highest Xe/Kr selectivity (69.7) but its working capacity is very low (only 0.25 mmol/g). Comparatively, our SIFSIX-6-Cd-i have moderate selectivity (16.4) but high working capacity (1.62 mmol/g).

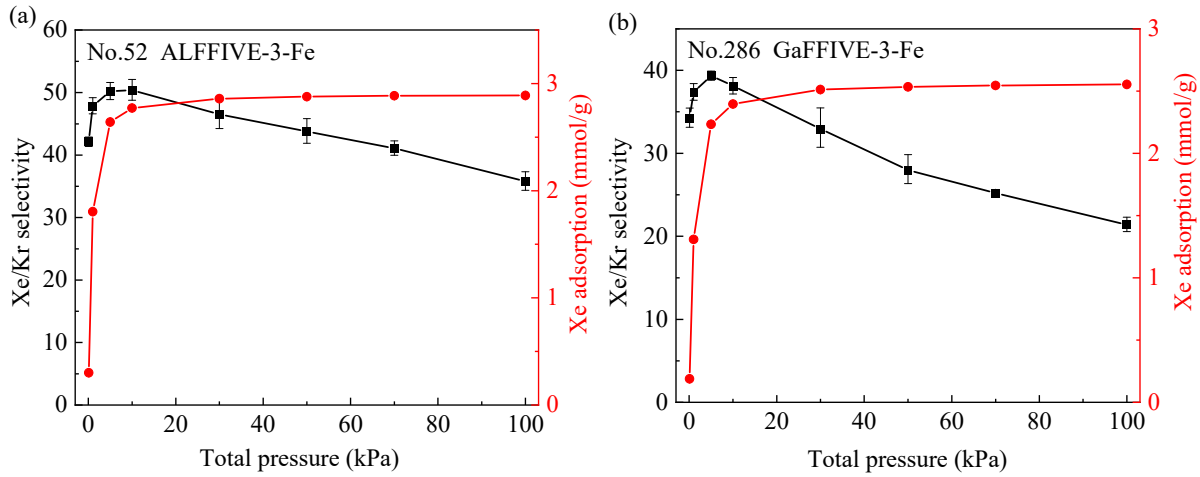

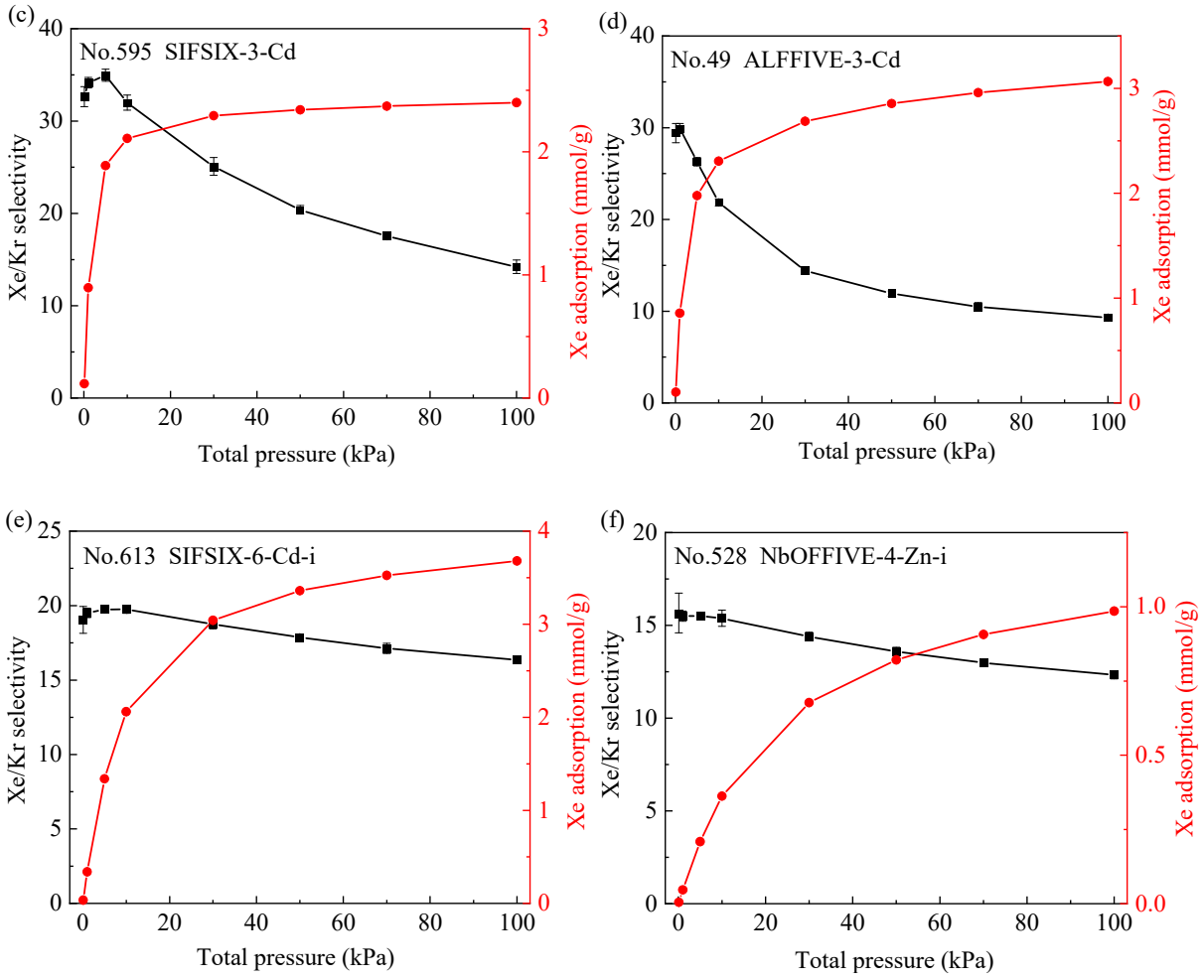

Figure 7: The separation selectivity of Xe/Kr (50/50) mixtures with total pressure from 0.1 to 100 kPa at 298 K for six MOFs from mixture GCMC simulations (a) ALFFIVE-3-Fe, (b) GaFFIVE-3-Fe, (c) SIFSIX-3-Cd, (d) ALFFIVE-3-Cd, (e) SIFSIX-6-Cd-i and (f) NbOFFIVE-4-Zn-i. The red line indicates the Xe uptake from Xe/Kr mixture. Numerical data is listed in Table S8.

Table 1. Xe/Kr selectivity for various porous materials at 298 K and 100 kPa.

Name	Selectivity $S_{Xe/Kr}$	Henry coefficient ratio	Working capacity (mmol/g)	Reference

$[Co_3(HCOO)_6]$	12[a]	8.7	1.18	[62]
Ni-MOF-74	5-6[a]	5.8	3.28	[63]
SB-MOF-1	16[a]	16.2	0.31	[64]
SB-MOF-2	10[a]	8.6	1.95	[65]
Cu-BTC	2.6[a]	8.5	1.47	[11]
FMOF-Cu	2[b]	1.4	0.40	[66]
MOF-505	9-10[c]	6.8	5.04	[67]
PAF-45S	24.1[d]	16.7	1.21	[68]
MOF-Cu-H	16.7[a]	15.8	0.37	[69]
CROFOUR-1-Ni	22[a]	24.3	0.98	[70]
CROFOUR-2-Ni	15.5[a]	18.5	0.90	[70]
NbOFFIVE-2-Cu-i	9.7[e]	-	3.21	[12]
$[Co_3(C_4O_4)_2(OH)_2]$	69.7[a]	51.4	0.25	[71]
ALFFIVE-3-Fe	35.8[f]	41.5	0.12	This work
GaFFIVE-3-Fe	21.4[f]	33.7	0.16	This work
SIFSIX-3-Cd	14.2[f]	32.5	0.29	This work
ALFFIVE-3-Cd	9.3[f]	29.2	0.76	This work
SIFSIX-6-Cd-i	16.4[f]	19.3	1.62	This work
NbOFFIVE-4-Zn-i	12.3[f]	15.6	0.62	This work

[a]Calculated by IAST. [b]From breakthrough experiment (Xe/Kr 50/50). [c]From breakthrough experiment with the Xe/Kr (20/80, v/v) mixture. [d]From breakthrough experiment (Xe 500 ppm, Kr 50 ppm). [e]Estimated by uptake ratio, Xe/Kr 0.2/0.8 bar, at 273 K. [f]Calculated by GCMC.

Simple Correlations of Xe and Kr Uptakes between Multivariate and Univariate MOFs. All of the MOFs considered above are univariate in the sense that each material only has a single kind of metal center and anion. In principle, these materials could also be made in a multivariate form where a single material includes a mixture of metal centers and/or anions. There are limited examples where this approach has been used to boost gas storage or separations, although there is no guarantee that a mixed material is superior to both of the "parent" single metal materials.[72] Motivated by these observations, we examined a limited number of examples of mixing metal centers and fluorine groups to probe the effects on Xe and Kr adsorption. Specifically, we performed calculations for $In_{0.125}Al_{0.875}$FFIVE-3-Fe, $In_{0.5}Al_{0.5}$FFIVE-3-Fe, $In_{0.875}Al_{0.125}$FFIVE-3-Fe, ALFFIVE-3-$Fe_{0.125}Cd_{0.875}$, ALFFIVE-3-$Fe_{0.5}Cd_{0.5}$ and ALFFIVE-3-$Fe_{0.875}Cd_{0.125}$ based on the parent univariate materials InFFIVE-3-Fe, ALFFIVE-3-Fe and ALFFIVE-3-Cd. Each material was structurally optimized using DFT with the same methods described above for a single ordering of the multivariate SBUs. Structural properties of the resulting MOFs are listed in Table 2. The heterogeneity of metal centers or fluorine groups can lead to the change of physical parameters like density, pore size, volume fraction and surface area of the parent MOFs. In some cases, for example, $In_{0.125}Al_{0.875}$FFIVE-3-Fe, $In_{0.5}Al_{0.5}$FFIVE-3-Fe and $In_{0.875}Al_{0.125}$FFIVE-3-Fe have higher PLD and volumetric surface area than both of the parent materials (InFFIVE-3-Fe and ALFFIVE-3-Fe).

GCMC simulations of single-component Xe and Kr adsorption at 298 K were then performed. The results for $In_{0.125}Al_{0.875}$FFIVE-3-Fe, $In_{0.5}Al_{0.5}$FFIVE-3-Fe, $In_{0.875}Al_{0.125}$FFIVE-3-Fe, InFFIVE-3-Fe and ALFFIVE-3-Fe are shown in Figure S3(a)-(b) and S4(a)-(b) to evaluate the effects of mixing fluorine groups. Similarly, the isotherms for ALFFIVE-3-$Fe_{0.125}Cd_{0.875}$, ALFFIVE-3-$Fe_{0.5}Cd_{0.5}$,

ALFFIVE-3-$Fe_{0.875}Cd_{0.125}$, ALFFIVE-3-Fe and ALFFIVE-3-Cd shown in Figure S3(c)-(d) and S4(c)-(d) indicate the impact of mixing metal centers.

The heterogeneity of metal centers or fluorine groups in MOFs can help to improve the Xe and Kr uptakes at medium pressure (30 – 100 kPa), as shown in Figure S3. This can be mainly attributed to the higher surface area of multivariate MOFs than that of the corresponding univariate one, as shown in Table 2. In addition, we also plotted the loading ratio of pure Xe/Kr at 10/10 kPa as a function of Xe working capacity at 10 - 100 kPa and 298 K for MOFs with mixed metal centers and mixed fluorine groups in Figure 8. The values of working capacity and Xe/Kr loading ratio for MOFs with mixed metal centers lie in the range of their corresponding parent materials. In the case of InFFIVE-3-Fe and ALFFIVE-3-Fe, the mixed form $In_{0.125}Al_{0.875}$FFIVE-3-Fe shows higher working capacity without a reduction in the Xe/Kr loading ratio. That means, heterogeneity of fluorine groups offers a potential route to improve practical Xe/Kr separation performance of these anion-pillared materials. The order of working capacity for parent MOFs in Figure 8 is AlFFIVE-3-Cd (0.89) > InFFIVE-3-Fe (0.18) > AlFFIVE-3-Fe (0.06), which is the same as order estimated above (AlFFIVE-3-Cd (0.32) > InFFIVE-3-Fe (0.16) > AlFFIVE-3-Fe (0.10)). This further validates the reliability of working capacity predictions made above with approximate isotherms. Previous work on adsorption in functionalized UiO-66 gives examples of how varying the chemical identity of substituents can influence adsorption properties.[73] This suggests that is may be possible to further adjust the Xe/Kr separations in anion-pillared MOFs by replacing fluorine with chlorine or with similar substitutions.

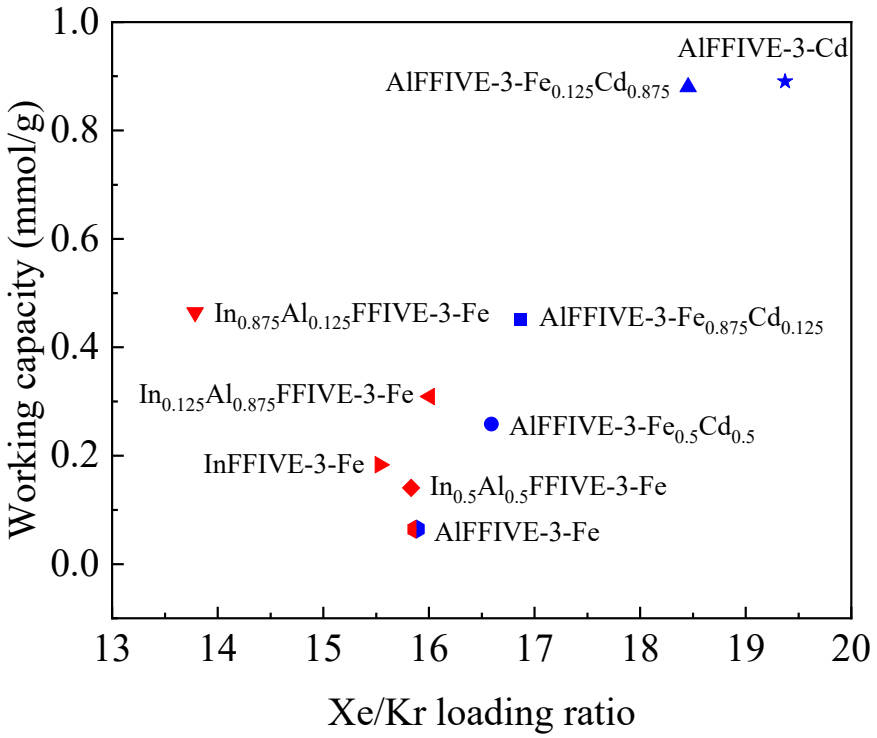

Figure 8: Plot of Xe/Kr loading ratio at 10/10 kPa as a function of Xe working capacity at 10 - 100 kPa and 298 K for MOFs with mixed metal centers and mixed fluorine groups. Numerical data is listed in Table S9.

Table 2. Physical parameters of multivariate and the corresponding univariate MOFs

Name	Density g/cm^3	PLD Å	LCD Å	Volume fraction		Surface area		
				Accessible	Occupiable	m^2/cm^3	m^2/g	Å^2
In$_{0.125}$Al$_{0.875}$FFIVE-3-Fe	1.41	3.70	4.97	0.061	0.285	1422	1008	3740
In$_{0.5}$Al$_{0.5}$FFIVE-3-Fe	1.51	3.49	4.83	0.060	0.283	1411	936	3797
In$_{0.875}$Al$_{0.125}$FFIVE-3-Fe	1.60	3.62	4.75	0.060	0.280	1430	894	3943
ALFFIVE-3-Fe$_{0.125}$Cd$_{0.875}$	1.45	3.95	5.24	0.077	0.314	1574	1086	4473
ALFFIVE-3-Fe$_{0.5}$Cd$_{0.5}$	1.48	3.65	4.87	0.059	0.286	1423	962	3745

ALFFIVE-3-$Fe_{0.875}Cd_{0.125}$	1.38	3.76	4.99	0.064	0.293	1447	1045	3831
InFFIVE-3-Fe	1.63	3.46	4.83	0.060	0.293	1408	865	2936
ALFFIVE-3-Fe	1.38	3.38	4.95	0.060	0.284	1377	996	3578
ALFFIVE-3-Cd	1.44	3.92	5.29	0.081	0.332	1603	1113	3499

■ CONCLUSION

This article reports a database of 936 anion-pillared MOFs derived from the available experimental structures. We optimized each structure with DFT and calculated various physical properties including density, ASA, PLD, LCD, probe-accessible and probe-occupiable volume fraction for each MOF. The structural properties vary more strongly with the choice of the organic ligand than with other aspects like fluorine groups and metal centers for MOFs. For example, the accessible surface area can be varied with increments of ~200 m^2/cm^3 by varying the organic ligand, but only increments of ~40 m^2/cm^3 by varying the fluorine groups or metal centers. We performed high-throughput screening on these 936 MOFs for Xe/Kr separation with three approximate metrics including the Henry coefficient ratio, working capacity and regenerability. Generally, the MOFs with higher Xe/Kr selectivity show lower working capacity and regenerability. GCMC simulations were carried out to evaluate the Xe/Kr separation performance of six promising MOFs suggested by the screening results. We compared the separation performance of these six anion-pillared MOFs with several previously reported MOFs. The SIFSIX-6-Cd-i material in our work strikes a good balance between working capacity and separation selectivity. Finally, we showed that the heterogeneity of fluorine groups can help to enhance Xe working capacity without reducing Xe/Kr selectivity in at least one example. This indicates that heterogeneity of fluorine groups can be a possible method to

improve Xe/Kr separation performance of anion-pillared MOFs. The potential of these materials for Xe/Kr separations suggests that they may also be interesting for a range of other gas separations.

■ ASSOCIATED CONTENT

Supporting Information

Experimental structures collected in this work; Ligand number and ligand name of MOFs in this database; Values of experimental and DFT optimized cell/bond lengths in Figure 3; Numerical data in Figure 4 and 6: Physical descriptors, Henry coefficient ratios, working capacities and regenerabilities for the MOFs in the database; 4 groups with only different in fluorine groups, metal centers, organic ligands and structural interpenetrations, respectively; Comparison of saturated Xe loadings from GCMC with predictions of our approximate method; Numerical data in Figure 7; The heat of adsorption and difference in heat of adsorption of Xe and Kr in binary gas adsorption; Adsorption of pure Xe and Kr in MOFs with mixed fluorine groups or mixed metal centers; Numerical data in Figure 8. (PDF)

Input files for geometry optimization of SIFSIX-2-Cu; Input files for interaction energy of single Xe and Kr atoms in SIFSIX-6-Cd-i; Input files for calculating Henry coefficients of pure Xe and Kr in SIFSIX-2-Cu at 298 K; Input files for calculating the adsorption of Xe/Kr mixtures in SIFSIX-6-Cd-i at 100 kPa and 298 K; 6 cif files for MOFs in Figure 7; Structures of 936 anion-pillared MOF structures. (ZIP)

■ AUTHOR INFORMATION

Corresponding Authors

*Email: liujing27@mail.hust.edu.cn. Phone: +86-27-87545526 (J.L.)

*E-mail: david.sholl@chbe.gatech.edu. Phone: 1-4048942822 (D.S.S.).

ORCID

Jing Liu: 0000-0001-6520-9612

David S. Sholl: 0000-0002-2771-9168

Notes

The authors declare no competing financial interest.

■ ACKNOWLEDGMENTS

This work was supported by Fundamental Research Funds for the Central Universities (2019kfyRCPY021), China Scholarship Council (201906160014). Z.Y. and D.S.S. received funding from the Center for Understanding and Control of Acid Gas-Induced Evolution of Materials for Energy (UNCAGE-ME), an Energy Frontier Research Center funded by the U.S. Department of Energy, Office of Science, Office of Basic Energy Sciences, under Award No. DE-SC0012577. We would like to thank Hanjun Fang and Dai Tang for technical help and useful discussions.

■ REFERENCES

(1) Lin, R.-B.; Xiang, S.; Zhou, W.; Chen, B. Microporous Metal-Organic Framework Materials for Gas Separation. *Chem.* **2020,** *6* (2), 337-363.

(2) Cui, X.; Yang, Q.; Yang, L.; Krishna, R.; Zhang, Z.; Bao, Z.; Wu, H.; Ren, Q.; Zhou, W.; Chen, B. Ultrahigh and Selective SO_2 Uptake in Inorganic Anion-Pillared Hybrid Porous Materials. *Adv. Mater.* **2017,** *29* (28), 1606929.

(3) Yang, L.; Cui, X.; Zhang, Y.; Wang, Q.; Zhang, Z.; Suo, X.; Xing, H. Anion Pillared Metal–Organic Framework Embedded with Molecular Rotors for Size-Selective Capture of CO_2 from CH_4 and N_2. *ACS Sustain. Chem. Eng.* **2019,** *7* (3), 3138-3144.

(4) Elsaidi, S. K.; Mohamed, M. H.; Simon, C. M.; Braun, E.; Pham, T.; Forrest, K. A.; Xu, W.; Banerjee, D.; Space, B.; Zaworotko, M. J.; Thallapally, P. K. Effect of Ring Rotation Upon Gas Adsorption in SIFSIX-3-M (M = Fe, Ni) Pillared Square Grid Networks. *Chem. Sci.* **2017,** *8* (3), 2373-2380.

(5) Yang, L.; Qian, S.; Wang, X.; Cui, X.; Chen, B.; Xing, H. Energy-Efficient Separation Alternatives: Metal–Organic Frameworks and Membranes for Hydrocarbon Separation. *Chem. Soc. Rev.* **2020,** *49* (15), 5359-5406.

(6) Lane, G. A.; Nahrwold, M. L.; Tait, A. R.; Taylor-Busch, M.; Cohen, P. J.; Beaudoin, A. R. Anesthetics as Teratogens: Nitrous Oxide Is Fetotoxic, Xenon Is Not. *Science* **1980,** *210* (4472), 899-901.

(7) Sholl, D. S.; Lively, R. P. Seven Chemical Separations to Change the World. *Nature* **2016,** *532* (7600), 435-437.

(8) Bazan, R.; Bastos-Neto, M.; Moeller, A.; Dreisbach, F.; Staudt, R. Adsorption Equilibria of O_2, Ar,

Kr and Xe on Activated Carbon and Zeolites: Single Component and Mixture Data. *Adsorption* **2011,** *17* (2), 371-383.

(9) Wang, Q.; Xiong, S.; Xiang, Z.; Peng, S.; Wang, X.; Cao, D. Dynamic Separation of Xe and Kr by Metal-Organic Framework and Covalent-Organic Materials: A Comparison with Activated Charcoal. *Sci. China Chem.* **2016,** *59* (5), 643-650.

(10) Thallapally, P. K.; Grate, J. W.; Motkuri, R. K. Facile Xenon Capture and Release at Room Temperature Using a Metal–Organic Framework: A Comparison with Activated Charcoal. *Chem. Commun.* **2012,** *48* (3), 347-349.

(11) Bae, Y.-S.; Hauser, B. G.; Colón, Y. J.; Hupp, J. T.; Farha, O. K.; Snurr, R. Q. High Xenon/Krypton Selectivity in a Metal-Organic Framework with Small Pores and Strong Adsorption Sites. *Micropor. Mesopor. Mat.* **2013,** *169*, 176-179.

(12) Wang, Q.; Ke, T.; Yang, L.; Zhang, Z.; Cui, X.; Bao, Z.; Ren, Q.; Yang, Q.; Xing, H. Separation of Xe from Kr with Record Selectivity and Productivity in Anion-Pillared Ultramicroporous Materials by Inverse Size-Sieving. *Angew. Chem. Int. Ed.* **2020,** *59* (9), 3423-3428.

(13) Cui, X.; Chen, K.; Xing, H.; Yang, Q.; Krishna, R.; Bao, Z.; Wu, H.; Zhou, W.; Dong, X.; Han, Y.; Li, B.; Ren, Q.; Zaworotko, M. J.; Chen, B. Pore Chemistry and Size Control in Hybrid Porous Materials for Acetylene Capture from Ethylene. *Science* **2016,** *353* (6295), 141-144.

(14) Brandani, S.; Farmahini, A. H.; Friedrich, D.; Krishnamurthy, S.; Sarkisov, L. Performance-Based Screening of Porous Materials for Carbon Capture. *arXiv preprint arXiv:2009.12289* **2020**.

(15) Baerlocher, C.; McCusker, L. Database of Zeolite Structures: http://www. iza-structure. org/databases. Accessed August 1, 2020.

(16) Knio, O.; Medford, A. J.; Nair, S.; Sholl, D. S. Database of Computation-Ready 2D Zeolitic Slabs. *Chem. Mater.* **2019,** *31* (2), 353-364.

(17) Thyagarajan, R.; Sholl, D. S. A Database of Porous Rigid Amorphous Materials. *Chem. Mater.* **2020,** *32* (18), 8020-8033.

(18) Groom, C. R.; Bruno, I. J.; Lightfoot, M. P.; Ward, S. C. The Cambridge Structural Database. *Acta Crystallogr. B* **2016,** *72* (2), 171-179.

(19) Chung, Y. G.; Camp, J.; Haranczyk, M.; Sikora, B. J.; Bury, W.; Krungleviciute, V.; Yildirim, T.; Farha, O. K.; Sholl, D. S.; Snurr, R. Q. Computation-Ready, Experimental Metal–Organic Frameworks: A Tool to Enable High-Throughput Screening of Nanoporous Crystals. *Chem. Mater.* **2014,** *26* (21), 6185-6192.

(20) Chung, Y. G.; Haldoupis, E.; Bucior, B. J.; Haranczyk, M.; Lee, S.; Zhang, H.; Vogiatzis, K. D.; Milisavljevic, M.; Ling, S.; Camp, J. S.; Slater, B.; Siepmann, J. I.; Sholl, D. S.; Snurr, R. Q. Advances, Updates, and Analytics for the Computation-Ready, Experimental Metal–Organic Framework Database: Core Mof 2019. *J. Chem. Eng. Data* **2019,** *64* (12), 5985-5998.

(21) Burd, S. D.; Ma, S.; Perman, J. A.; Sikora, B. J.; Snurr, R. Q.; Thallapally, P. K.; Tian, J.; Wojtas, L.; Zaworotko, M. J. Highly Selective Carbon Dioxide Uptake by $[Cu(bpy\text{-}n)_2(SiF_6)]$ (bpy-1 = 4,4′-Bipyridine; bpy-2 = 1,2-Bis(4-pyridyl)ethene). *J. Am. Chem. Soc.* **2012,** *134* (8), 3663-3666.

(22) Gee, J. A.; Sholl, D. S. Characterization of the Thermodynamic Stability of Solvated Metal–Organic Framework Polymorphs Using Molecular Simulations. *J. Phys. Chem. C* **2013,** *117* (40), 20636-20642.

(23) Blöchl, P. E. Projector Augmented-Wave Method. *Phys. Rev. B* **1994,** *50* (24), 17953-17979.

(24) Kresse, G.; Furthmüller, J. Efficient Iterative Schemes for Ab Initio Total-Energy Calculations

Using a Plane-Wave Basis Set. *Phys. Rev. B* **1996,** *54* (16), 11169-11186.

(25) Nazarian, D.; Ganesh, P.; Sholl, D. S. Benchmarking Density Functional Theory Predictions of Framework Structures and Properties in a Chemically Diverse Test Set of Metal–Organic Frameworks. *J. Mater. Chem. A* **2015,** *3* (44), 22432-22440.

(26) Perdew, J. P.; Burke, K.; Ernzerhof, M. Generalized Gradient Approximation Made Simple. *Phys. Rev. Lett.* **1996,** *77* (18), 3865-3868.

(27) Grimme, S.; Antony, J.; Ehrlich, S.; Krieg, H. A Consistent and Accurate Ab Initio Parametrization of Density Functional Dispersion Correction (DFT-D) for the 94 Elements H-Pu. *J. Chem. Phys.* **2010,** *132* (15), 154104.

(28) Hautier, G.; Ong, S. P.; Jain, A.; Moore, C. J.; Ceder, G. Accuracy of Density Functional Theory in Predicting Formation Energies of Ternary Oxides from Binary Oxides and Its Implication on Phase Stability. *Phys. Rev. B* **2012,** *85* (15), 155208.

(29) Puigdollers, A. R.; Schlexer, P.; Pacchioni, G. Gold and Silver Clusters on TiO_2 and ZrO_2 (101) Surfaces: Role of Dispersion Forces. *J. Phys. Chem. C* **2015,** *119* (27), 15381-15389.

(30) Grajciar, L.; Nachtigall, P.; Bludský, O.; Rubeš, M. Accurate Ab Initio Description of Adsorption on Coordinatively Unsaturated Cu^{2+} and Fe^{3+} Sites in Mofs. *J. Chem. Theory Comput.* **2015,** *11* (1), 230-238.

(31) Dubbeldam, D.; Calero, S.; Ellis, D. E.; Snurr, R. Q. Raspa: Molecular Simulation Software for Adsorption and Diffusion in Flexible Nanoporous Materials. *Mol Simulat.* **2016,** *42* (2), 81-101.

(32) Hirschfelder, J. O.; Curtiss, C. F.; Bird, R. B.; Mayer, M. G. *Molecular Theory of Gases and Liquids*, Wiley New York: 1964; Vol. 165.

(33) Talu, O.; Myers, A. L. Reference Potentials for Adsorption of Helium, Argon, Methane, and

Krypton in High-Silica Zeolites. *Colloid. Surface. A* **2001,** *187-188*, 83-93.

(34) Rappé, A. K.; Casewit, C. J.; Colwell, K.; Goddard III, W. A.; Skiff, W. M. UFF, a Full Periodic Table Force Field for Molecular Mechanics and Molecular Dynamics Simulations. *J. Am. Chem. Soc.* **1992,** *114* (25), 10024-10035.

(35) Mayo, S. L.; Olafson, B. D.; Goddard, W. A. DREIDING: A Generic Force Field for Molecular Simulations. *J. Phys. Chem.* **1990,** *94* (26), 8897-8909.

(36) Bajpai, A.; O'Nolan, D.; Madden, D. G.; Chen, K.-J.; Pham, T.; Kumar, A.; Lusi, M.; Perry, J. J.; Space, B.; Zaworotko, M. J. The Effect of Centred Versus Offset Interpenetration on C_2H_2 Sorption in Hybrid Ultramicroporous Materials. *Chem. Commun.* **2017,** *53* (84), 11592-11595.

(37) Nugent, P.; Rhodus, V.; Pham, T.; Tudor, B.; Forrest, K.; Wojtas, L.; Space, B.; Zaworotko, M. Enhancement of CO_2 Selectivity in a Pillared pcu MOM Platform through Pillar Substitution. *Chem. Commun.* **2013,** *49* (16), 1606-1608.

(38) Lin, M.-J.; Jouaiti, A.; Kyritsakas, N.; Hosseini, M. W. Molecular Tectonics: Control of Interpenetration in Cuboid 3-D Coordination Networks. *CrystEngComm* **2011,** *13* (3), 776-778.

(39) Nugent, P.; Belmabkhout, Y.; Burd, S. D.; Cairns, A. J.; Luebke, R.; Forrest, K.; Pham, T.; Ma, S.; Space, B.; Wojtas, L.; Eddaoudi, M.; Zaworotko, M. J. Porous Materials with Optimal Adsorption Thermodynamics and Kinetics for CO_2 Separation. *Nature* **2013,** *495* (7439), 80-84.

(40) Shekhah, O.; Belmabkhout, Y.; Chen, Z.; Guillerm, V.; Cairns, A.; Adil, K.; Eddaoudi, M. Made-to-Order Metal-Organic Frameworks for Trace Carbon Dioxide Removal and Air Capture. *Nat. Commun.* **2014,** *5* (1), 4228.

(41) Wen, H.-M.; Liao, C.; Li, L.; Alsalme, A.; Alothman, Z.; Krishna, R.; Wu, H.; Zhou, W.; Hu, J.; Chen, B. A Metal–Organic Framework with Suitable Pore Size and Dual Functionalities for Highly

Efficient Post-Combustion CO_2 Capture. *J. Mater. Chem. A* **2019,** *7* (7), 3128-3134.

(42) Jiang, M.; Cui, X.; Yang, L.; Yang, Q.; Zhang, Z.; Yang, Y.; Xing, H. A Thermostable Anion-Pillared Metal-Organic Framework for C_2H_2/C_2H_4 and C_2H_2/CO_2 Separations. *Chem. Eng. J.* **2018,** *352*, 803-810.

(43) Yang, L.; Cui, X.; Zhang, Y.; Yang, Q.; Xing, H. A Highly Sensitive Flexible Metal–Organic Framework Sets a New Benchmark for Separating Propyne from Propylene. *J. Mater. Chem. A* **2018,** *6* (47), 24452-24458.

(44) Cadiau, A.; Belmabkhout, Y.; Adil, K.; Bhatt, P. M.; Pillai, R. S.; Shkurenko, A.; Martineau-Corcos, C.; Maurin, G.; Eddaoudi, M. Hydrolytically Stable Fluorinated Metal-Organic Frameworks for Energy-Efficient Dehydration. *Science* **2017,** *356* (6339), 731-735.

(45) Li, B.; Cui, X.; O'Nolan, D.; Wen, H.-M.; Jiang, M.; Krishna, R.; Wu, H.; Lin, R.-B.; Chen, Y.-S.; Yuan, D.; Xing, H.; Zhou, W.; Ren, Q.; Qian, G.; Zaworotko, M. J.; Chen, B. An Ideal Molecular Sieve for Acetylene Removal from Ethylene with Record Selectivity and Productivity. *Adv. Mater.* **2017,** *29* (47), 1704210.

(46) Yang, L.; Cui, X.; Yang, Q.; Qian, S.; Wu, H.; Bao, Z.; Zhang, Z.; Ren, Q.; Zhou, W.; Chen, B.; Xing, H. A Single-Molecule Propyne Trap: Highly Efficient Removal of Propyne from Propylene with Anion-Pillared Ultramicroporous Materials. *Adv. Mater.* **2018,** *30* (10), 1705374.

(47) Bajpai, A.; Lusi, M.; Zaworotko, M. J. The Role of Weak Interactions in Controlling the Mode of Interpenetration in Hybrid Ultramicroporous Materials. *Chem. Commun.* **2017,** *53* (28), 3978-3981.

(48) Zhang, Z.; Ding, Q.; Peh, S. B.; Zhao, D.; Cui, J.; Cui, X.; Xing, H. Mechano-Assisted Synthesis of an Ultramicroporous Metal–Organic Framework for Trace CO_2 Capture. *Chem.*

Commun. **2020,** *56* (56), 7726-7729.

(49) Mukherjee, S.; Sikdar, N.; O'Nolan, D.; Franz, D. M.; Gascón, V.; Kumar, A.; Kumar, N.; Scott, H. S.; Madden, D. G.; Kruger, P. E.; Space, B.; Zaworotko, M. J. Trace CO_2 Capture by an Ultramicroporous Physisorbent with Low Water Affinity. *Sci. Adv.* **2019,** *5* (11), eaax9171.

(50) Manz, T. A.; Sholl, D. S. Chemically Meaningful Atomic Charges That Reproduce the Electrostatic Potential in Periodic and Nonperiodic Materials. *J. Chem. Theory Comput.* **2010,** *6* (8), 2455-2468.

(51) Willems, T. F.; Rycroft, C. H.; Kazi, M.; Meza, J. C.; Haranczyk, M. Algorithms and Tools for High-Throughput Geometry-Based Analysis of Crystalline Porous Materials. *Micropor. Mesopor. Mat.* **2012,** *149* (1), 134-141.

(52) Fang, H.; Kamakoti, P.; Zang, J.; Cundy, S.; Paur, C.; Ravikovitch, P. I.; Sholl, D. S. Prediction of CO_2 Adsorption Properties in Zeolites Using Force Fields Derived from Periodic Dispersion-Corrected DFT Calculations. *J. Phys. Chem. C* **2012,** *116* (19), 10692-10701.

(53) Fang, H.; Awati, R.; Boulfelfel, S. E.; Ravikovitch, P. I.; Sholl, D. S. First-Principles-Derived Force Fields for CH_4 Adsorption and Diffusion in Siliceous Zeolites. *J. Phys. Chem. C* **2018,** *122* (24), 12880-12891.

(54) Fang, H.; Demir, H.; Kamakoti, P.; Sholl, D. S. Recent Developments in First-Principles Force Fields for Molecules in Nanoporous Materials. *J. Mater. Chem. A* **2014,** *2* (2), 274-291.

(55) Park, J.; Rubiera Landa, H. O.; Kawajiri, Y.; Realff, M. J.; Lively, R. P.; Sholl, D. S. How Well Do Approximate Models of Adsorption-Based CO_2 Capture Processes Predict Results of Detailed Process Models? *Ind. Eng. Chem. Res.* **2020,** *59* (15), 7097-7108.

(56) Bae, Y. S.; Snurr, R. Q. Development and Evaluation of Porous Materials for Carbon Dioxide

Separation and Capture. *Angew. Chem. Int. Ed.* **2011,** *50* (49), 11586-11596.

(57) Wilmer, C. E.; Farha, O. K.; Bae, Y.-S.; Hupp, J. T.; Snurr, R. Q. Structure–Property Relationships of Porous Materials for Carbon Dioxide Separation and Capture. *Energ. Environ. Sci.* **2012,** *5* (12), 9849-9856.

(58) Chung, Y. G.; Gómez-Gualdrón, D. A.; Li, P.; Leperi, K. T.; Deria, P.; Zhang, H.; Vermeulen, N. A.; Stoddart, J. F.; You, F.; Hupp, J. T. In Silico Discovery of Metal-Organic Frameworks for Precombustion CO_2 Capture Using a Genetic Algorithm. *Sci. Adv.* **2016,** *2* (10), e1600909.

(59) Walton, K. S.; Sholl, D. S. Predicting Multicomponent Adsorption: 50 Years of the Ideal Adsorbed Solution Theory. *AlChE J.* **2015,** *61* (9), 2757-2762.

(60) Tang, D.; Wu, Y.; Verploegh, R. J.; Sholl, D. S. Efficiently Exploring Adsorption Space to Identify Privileged Adsorbents for Chemical Separations of a Diverse Set of Molecules. *ChemSusChem* **2018,** *11* (9), 1567-1575.

(61) Altintas, C.; Avci, G.; Daglar, H.; Nemati Vesali Azar, A.; Velioglu, S.; Erucar, I.; Keskin, S. Database for CO_2 Separation Performances of Mofs Based on Computational Materials Screening. *ACS Appl. Mater. Inter.* **2018,** *10* (20), 17257-17268.

(62) Wang, H.; Yao, K.; Zhang, Z.; Jagiello, J.; Gong, Q.; Han, Y.; Li, J. The First Example of Commensurate Adsorption of Atomic Gas in a Mof and Effective Separation of Xenon from Other Noble Gases. *Chem. Sci.* **2014,** *5* (2), 620-624.

(63) Liu, J.; Thallapally, P. K.; Strachan, D. Metal–Organic Frameworks for Removal of Xe and Kr from Nuclear Fuel Reprocessing Plants. *Langmuir* **2012,** *28* (31), 11584-11589.

(64) Banerjee, D.; Simon, C. M.; Plonka, A. M.; Motkuri, R. K.; Liu, J.; Chen, X.; Smit, B.; Parise, J. B.; Haranczyk, M.; Thallapally, P. K. Metal–Organic Framework with Optimally Selective Xenon

Adsorption and Separation. *Nat. Commun.* **2016,** *7* (1), 1-7.

(65) Chen, X.; Plonka, A. M.; Banerjee, D.; Krishna, R.; Schaef, H. T.; Ghose, S.; Thallapally, P. K.; Parise, J. B. Direct Observation of Xe and Kr Adsorption in a Xe-Selective Microporous Metal–Organic Framework. *J. Am. Chem. Soc.* **2015,** *137* (22), 7007-7010.

(66) Fernandez, C. A.; Liu, J.; Thallapally, P. K.; Strachan, D. M. Switching Kr/Xe Selectivity with Temperature in a Metal–Organic Framework. *J. Am. Chem. Soc.* **2012,** *134* (22), 9046-9049.

(67) Ryan, P.; Farha, O. K.; Broadbelt, L. J.; Snurr, R. Q. Computational Screening of Metal-Organic Frameworks for Xenon/Krypton Separation. *AlChE J.* **2011,** *57* (7), 1759-1766.

(68) Li, J.; Huang, L.; Zou, X.; Zheng, A.; Li, H.; Rong, H.; Zhu, G. Porous Organic Materials with Ultra-Small Pores and Sulfonic Functionality for Xenon Capture with Exceptional Selectivity. *J. Mater. Chem. A* **2018,** *6* (24), 11163-11168.

(69) Xiong, S.; Gong, Y.; Hu, S.; Wu, X.; Li, W.; He, Y.; Chen, B.; Wang, X. A Microporous Metal–Organic Framework with Commensurate Adsorption and Highly Selective Separation of Xenon. *J. Mater. Chem. A* **2018,** *6* (11), 4752-4758.

(70) Mohamed, M. H.; Elsaidi, S. K.; Pham, T.; Forrest, K. A.; Schaef, H. T.; Hogan, A.; Wojtas, L.; Xu, W.; Space, B.; Zaworotko, M. J.; Thallapally, P. K. Hybrid Ultra-Microporous Materials for Selective Xenon Adsorption and Separation. *Angew. Chem. Int. Ed.* **2016,** *55* (29), 8285-8289.

(71) Li, L.; Guo, L.; Zhang, Z.; Yang, Q.; Yang, Y.; Bao, Z.; Ren, Q.; Li, J. A Robust Squarate-Based Metal–Organic Framework Demonstrates Record-High Affinity and Selectivity for Xenon over Krypton. *J. Am. Chem. Soc.* **2019,** *141* (23), 9358-9364.

(72) You, W.; Sen, T.; Kawajiri, Y.; Realff, M. J.; Sholl, D. S. Using Site Heterogeneity in Metal–Organic Frameworks with Bimetallic Open Metal Sites for Olefin/Paraffin Separations. *ACS Appl.*

Nano Mater. **2020,** *3* (6), 5291-5300.

(73) Demir, H.; Walton, K. S.; Sholl, D. S. Computational Screening of Functionalized UiO-66 Materials for Selective Contaminant Removal from Air. *J. Phys. Chem. C* **2017,** *121* (37), 20396-20406.

Table Of Contents (TOC) graphic